



Cite this: *Phys. Chem. Chem. Phys.*,  
2018, 20, 7295

## Reverse electrodialysis in bilayer nanochannels: salinity gradient-driven power generation

Rui Long, \* Zhengfei Kuang, Zhichun Liu and Wei Liu\*

To evaluate the possibility of nano-fluidic reverse electrodialysis (RED) for salinity gradient energy harvesting, we consider the behavior of ion transportation in a bilayer cylindrical nanochannel consisting of different sized nanopores connecting two large reservoirs at different NaCl concentrations. Numerical simulations to illustrate the electrokinetic behavior at asymmetric sub-pore length and surface charge density are conducted, the impacts of which on transference number, osmotic current, diffusive voltage, maximum power and maximum power efficiency are systematically investigated. The results reveal that the transference number in Config. I (where high NaCl concentration is applied at the larger nanopore) is always larger than that in the opposite configuration (Config. II). At low concentration ratios, the osmotic current and maximum power have maximum values, while the maximum power efficiency decreases consistently. For Config. II, the ion transportation is impacted by the surface charge density at both sub-nanopores, while for Config. I, it is determined by the surface charge density at the downstream small nanopore. When large surface charge density is applied at the downstream small nanopore in contact with a very low concentration reservoir, there exists an interesting phenomenon: the larger surface charge density at the large nanopore induces a slight performance drop due to the impact of upstream EDL overlap.

Received 15th December 2017,  
Accepted 19th February 2018

DOI: 10.1039/c7cp08394g

rsc.li/pccp

### 1. Introduction

Due to the combustion of traditional fossil fuels, the environment suffers from effects such as mass haze, which induces severe respiratory disease, and global warming, which leads to rising sea levels and animal extinction.<sup>1</sup> Exploiting green and new energy substitutes and developing efficient energy utilization methods contribute to relieving such issues, such as thermally regenerative electrochemical cycles for recovery of low grade waste,<sup>2,3</sup> reverse electrodialysis (RED) and pressure retarded osmosis (PRO) for harvesting salinity gradient energy,<sup>4–7</sup> and piezoelectric devices for utilizing vibration energy.<sup>8</sup> Salinity gradient energy derives from the mixing of sea water and river water, and could be a promising energy source in the future due to its high availability. PRO and RED are the main technologies for utilizing salinity gradient energy, and the latter is attracting increasing interest due to its lower demand on the system and the reliability of miniaturization.<sup>9</sup>

Recently nano-fluidic RED has drawn increasing attention due to its much greater power density compared to traditional macro RED systems.<sup>10,11</sup> In nano-fluidic RED systems, a nanopore connects two salt solution reservoirs at different concentrations,

inducing a concentration gradient that drives the ionic species from the high concentration reservoir to the low concentration one. The nanopore is usually positively or negatively charged so as to be ion selective, therefore counter-ions are attracted and co-ions are expelled due to the electrostatic effect, and an electrical double layer (EDL) is formed adjacent to the channel surface. Furthermore, a diffusive current is established when a concentration gradient is applied at the nanopore ends, which can offer external power supply by converting the Gibbs free energy into electricity. Gao *et al.*<sup>12</sup> reported a nano-fluidic device with an asymmetric ionic diode membrane, and a power density of up to 3.46 W m<sup>-2</sup> was obtained. Kim *et al.*<sup>13</sup> investigated the power generation from silica nanochannels *via* KCl solutions and a power density of 7.7 W m<sup>-2</sup> was measured. Furthermore, a power generation of 543 nW was exacted from an alumina nanopore array with a nominal pore radius of 10 nm using NaCl solutions.<sup>14</sup>

Along with the experimental efforts, models have been developed to simulate the ion transfer characteristics in the charged nanochannels, thus providing fundamental explanations of the experimental results and offering guidance for designing and optimizing nano-fluidic RED systems.<sup>15</sup> Poisson–Nernst–Planck (PNP) equations, which are widely adopted for numerical simulations of RED/ED in nanopores, do not include the electrical neutrality assumption and show great agreement with experimental results.<sup>16–20</sup> Yeh *et al.*<sup>21</sup> investigated the RED process in negatively charged conical nanopores using the PNP equations.

School of Energy and Power Engineering, Huazhong University of Science and Technology, 1037 Luoyu Road, Wuhan 430074, China. E-mail: r\_long@hust.edu.cn, w\_liu@hust.edu.cn; Fax: +86-27-87540724; Tel: +86-27-87542618

Via the same model, Hsu *et al.*<sup>22</sup> further considered the pH regulated surface charge on conical nanopores. The PNP models can also be applied in the simulation of ion transference characteristics in asymmetric and complex nanopores.<sup>10,23</sup>

The performance of nano-fluidic RED devices is mainly impacted by the concentration gradient, nanopore geometry, temperature, and electrolyte type. Yeh *et al.*<sup>24</sup> found that a reversed ion selectivity of the nanopore occurred at a sufficiently large gradient. Hwang *et al.*<sup>23</sup> investigated the temperature sensitivity of the nano-fluidic RED performance using an MPS thin film with a pore diameter of 2–3 nm, and revealed that a temperature increase improves the ion conductance. Tseng *et al.*<sup>25</sup> analysed the influences of temperature and nanopore size and found that the maximum power increases with increasing temperature. Cao *et al.*<sup>26</sup> systematically investigated the nano-fluidic RED performance in relation to the electrolyte type and the charge selectivity, and illustrated that the power extracted and energy efficiency can be significantly improved with well-matched electrolyte types and nanopore charge selectivity. Kang *et al.*<sup>27</sup> adopted an anodic alumina nanopore for nano-fluidic power generation, and a power density of  $9.9 \text{ W m}^{-2}$  was achieved.

In previous literature, the performance of nano-fluidic RED in cylindrical and conical-shaped nanopores has been systematically investigated. Other forms of nanopores are rarely considered, especially bilayer nanochannels where the channel contains different sized nanopores, which have shown their potential of improving the ion selectivity due to their special geometry. Zhang *et al.*<sup>28</sup> investigated a tailor-made Janus membrane with bilayer nanopores of different radii at opposite surface charge densities for nano-fluidic RED, and claimed that the power density could approach  $10 \text{ W m}^{-2}$  by increasing the utilization rate of the pores in the functional layer. However, since the

varied asymmetric surface charge densities and nanopore lengths in the bilayer nanochannel were not examined, the underlying mechanisms were not sufficiently discussed. Accordingly, the present study is focused on numerical simulations to examine the electrokinetic behavior of a bilayer nanochannel consisting of different sized nanopores based on the PNP equations and Navier–Stoke equations. The influences of the ionic direction, reservoir salt concentration ratio, asymmetric sub-nanopore length and surface charge density on the transference number, diffusive voltage, osmotic current, maximum power, and maximum power density are investigated systematically, and the underlying mechanisms are discussed in detail. The results could provide useful information to improve the performance of nano-fluidic RED in bilayer nanopores.

## 2. Theory

As depicted in Fig. 1(a) and (b), we consider a cylindrical bilayer nanochannel consisting of sub-nanopores with radius  $R_1 = 5 \text{ nm}$  and  $R_2 = 10 \text{ nm}$ , and length  $L_1$  and  $L_2$  ( $L_1 + L_2 = 800 \text{ nm}$ ), respectively. The bilayer nanochannel connects two identical large cylindrical reservoirs (NaCl aqueous solution) of radius  $R_r = 500 \text{ nm}$  and length  $L_r = 500 \text{ nm}$ . The walls of the nanopores in the bilayer channel are negatively charged with constant charge densities of  $\sigma_1$  and  $\sigma_2$ . Due to the asymmetry of the geometry, two configurations are considered. In Config. I, high NaCl concentration is employed in the reservoir in contact with the larger pore, and in Config. II, high NaCl concentration is in the reservoir in contact with the small pore. The high (low) concentration of the reservoir is denoted  $C_H$  ( $C_L$ ).

The continuum based model, coupling PNP equations and Navier–Stokes equations, is employed to illustrate the electrostatics,

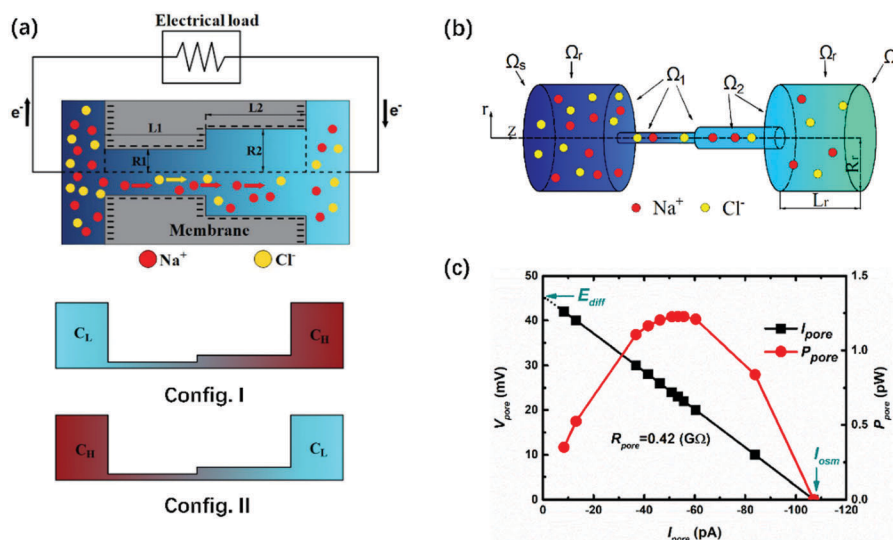


**Fig. 1** (a) Schematic of the salinity gradient energy harvesting system with a cylindrical bilayer nanochannel, consisting of two different sized sub-nanopores, which connects two identical large cylindrical reservoirs. Due to the asymmetric geometry of the bilayer nanochannel, there exists two configurations for ion transportation. In Config. I, high NaCl concentration is employed in the reservoir in contact with the large pore; in Config. II, high NaCl concentration is in the reservoir in contact with the small pore. (b) Illustration of the boundary conditions of the different domains or sub-domains. (c) The current–voltage curve and current–power curve for Config. I are plotted at  $C_L = 1 \text{ mM}$ ,  $C_H = 50 \text{ mM}$ ,  $\sigma_1 = \sigma_2 = 10 \text{ mC m}^{-2}$  and  $L_1 = L_2 = 400 \text{ nm}$ .

ionic mass transport and hydrodynamics process, and the equations are summarized below.

$$-\varepsilon \nabla^2 \phi = F(z_1 c_1 + z_2 c_2) \quad (1)$$

$$\nabla \cdot \mathbf{J}_i = 0, \quad \text{where } \mathbf{J}_i = c_i \mathbf{u} - D_i \nabla c_i - \frac{D_i z_i F c_i}{RT} \nabla \phi \quad (2)$$

$$-\nabla p + \mu \nabla^2 \mathbf{u} - F(z_1 c_1 + z_2 c_2) \nabla \phi = 0 \quad (3)$$

$$\nabla \cdot \mathbf{u} = 0 \quad (4)$$

where  $\phi$  is the electrical potential.  $\mathbf{J}_i$ ,  $c_i$ ,  $D_i$  and  $z_i$  are the ionic flux, concentration, diffusivity, and valence of the  $i$ th ionic species, respectively ( $i = 1$  for  $\text{Na}^+$  and  $i = 2$  for  $\text{Cl}^-$ ).  $F$ ,  $R$  and  $T$  are the Faraday constant, universal gas constant and temperature, respectively.  $\mu$  is the viscosity.  $\varepsilon$ ,  $p$ , and  $\mathbf{u}$  are the permittivity, pressure, and velocity of the fluid, respectively.

We solve the above equations numerically using the commercial Multiphysics software COMSOL subject to the following boundary conditions:

$$-\varepsilon \mathbf{n} \cdot \nabla \phi = 0 \quad \text{on } \Omega_r \text{ and } \Omega_s \quad (5)$$

$$-\varepsilon \mathbf{n} \cdot \nabla \phi = \sigma_1 \quad \text{on } \Omega_1 \quad (6)$$

$$-\varepsilon \mathbf{n} \cdot \nabla \phi = \sigma_2 \quad \text{on } \Omega_2 \quad (7)$$

$$\mathbf{n} \cdot \mathbf{J}_i = 0 \quad \text{on } \Omega_r \text{ and } \Omega_s \quad (8)$$

where  $\mathbf{n}$  is the normal vector and  $\Omega_1$ ,  $\Omega_2$  and  $\Omega_r$  are the surface of the small nanopore, large nanopore, and the reservoir, respectively.  $\Omega_s$  denotes the end faces of the reservoirs.

The electrical current through the bilayer nanopore,  $I$ , can be calculated using

$$I = \int_A F \left( \sum_i^2 z_i \mathbf{J}_i \right) \cdot \mathbf{n} dA \quad (9)$$

where  $A$  represents either end of the reservoirs.

When no external potential bias is applied between the reservoir surfaces, the osmotic current ( $I_{\text{osm}}$ ) can be calculated using  $I_{\text{osm}} = I_+ + I_-$ , where  $I_+$  and  $I_-$  are the electrical currents contributed by the cations and anions, respectively. The transference number  $t_+$  indicating the bilayer channel selectivity is calculated using

$$t_+ = \frac{I_+}{I_+ + |I_-|} \quad (10)$$

Originating from the selectivity, a diffusion potential across the bilayer channel,  $E_{\text{diff}}$ , is formed<sup>13</sup>

$$E_{\text{diff}} = (2t_+ - 1) \frac{RT}{zF} \ln \left( \frac{\gamma_{\text{H}} C_{\text{H}}}{\gamma_{\text{L}} C_{\text{L}}} \right) \quad (11)$$

where  $\gamma_{\text{H}}$  and  $\gamma_{\text{L}}$  are the activity coefficient of the high and low concentration solutions, which can be calculated using<sup>29</sup>

$$\log \left( \gamma_{\text{H(L)}}^{1/z_+ z_-} \right) = \frac{-0.511 I_s^{1/2}}{1 + I_s^{1/2}} + \frac{(0.06 + 0.03444) I_s}{\left( 1 + \frac{1.5}{|z_+ z_-|} I_s \right)^2} + \frac{0.0574 I_s}{|z_+ z_-|} \quad (12)$$

where  $I_s$  is the ionic strength.

### 3. Results and discussion

The behaviour of the system was examined using numerical simulations by varying the sub-nanopore length, surface charge density, and NaCl concentration in the high concentration reservoir, using COMSOL based on the finite element method with quadrilateral elements and refined meshes between *ca.* 180 000 and *ca.* 240 000 elements. The calculation results are confirmed to be grid independent by solutions obtained from denser meshes, where the minimum element size is less than 0.15 nm. The relevant parameters for calculation are listed as follows:  $T = 298$  K,  $\varepsilon_{\text{f}} = 7.08 \times 10^{-10}$  F m<sup>-1</sup>,  $F = 96 490$  C mol<sup>-1</sup>,  $D(\text{Cl}^-) = 2.032 \times 10^{-9}$  m<sup>2</sup> s<sup>-1</sup>,  $\mu = 0.001$  Pa s, and  $D(\text{Na}^+) = 1.334 \times 10^{-9}$  m<sup>2</sup> s<sup>-1</sup>.

As shown in Fig. 1(c), the electrical current has a linear relationship with the voltage, demonstrating the Ohm's behavior of the conduction current with a constant internal resistance of  $R_{\text{pore}} = 0.42$  G $\Omega$ . The electrical power ( $P_{\text{pore}}$ ) is the product of the ionic current ( $I_{\text{pore}}$ ) and the voltage ( $V_{\text{pore}}$ ), that is  $P_{\text{pore}} = I_{\text{pore}} V_{\text{pore}}$ , and it achieves its maximum value,  $P_{\text{max}} = I_{\text{osm}} V_{\text{diff}}/4$ , at  $V_{\text{pore}} = V_{\text{diff}}/2$  and  $I_{\text{pore}} = I_{\text{osm}}/2$ .

The energy efficiency is defined as the ratio of the electrical power to the Gibbs free energy of mixing,<sup>25</sup> and can be calculated using

$$\eta = \frac{I \Delta V}{(J_+ + J_-) RT \ln \left( \frac{\gamma_{\text{H}} C_{\text{H}}}{\gamma_{\text{L}} C_{\text{L}}} \right)} \quad (13)$$

where  $J_+$  and  $J_-$  are the fluxes of cations and anions, respectively. The efficiency corresponding to the maximum power is<sup>25</sup>

$$\eta_{\text{max power}} = \frac{(2t_+ - 1)^2}{2} \quad (14)$$

#### Impacts of ionic diffusion direction

Fig. 2 shows the axial concentration distribution for different ionic diffusion directions (Config. I and Config. II) at various concentration ratios. The bilayer nanochannel consists of a 400 nm cylindrical nanopore with a radius of 5 nm and a 400 nm cylindrical nanopore with a radius of 10 nm. In the calculation,  $C_{\text{L}}$  is fixed at 1 mM and  $C_{\text{H}}$  varies from 10 mM to 1000 mM, exponentially. The surface charge densities at the sub-nanopores are  $\sigma_1 = \sigma_2 = 10$  mC m<sup>-2</sup>. As the thickness of the electrical double layer (EDL) is determined by the Debye length  $\lambda_{\text{D}} \propto 1/\sqrt{C}$ , where  $C$  is the local concentration, the lower the concentration, the larger the EDL thickness and the larger the degree of EDL overlap. When the nanopore radius increases, the EDL overlap becomes less significant as the Debye length is much smaller than the pore radius. For Config. I, the concentration of  $\text{Na}^+$  shows an obvious jump at the nanopore junction due to the significant impact of the EDL overlap in the downstream small pore. With an increase of the reservoir concentration, the EDL thickness is reduced, and the ion transportation driven by the concentration gradient becomes more dominant. Therefore, at high concentration ratios, the concentration of  $\text{Cl}^-$  approaches that of  $\text{Na}^+$ . This phenomenon first takes place in the nanopore with  $R = 10$  nm,

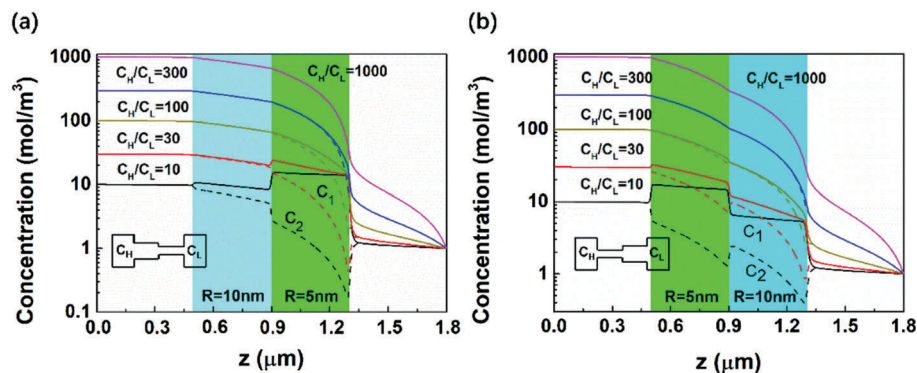


Fig. 2 Axial concentration distribution for different ionic diffusion directions (Config. I and Config. II) at various concentration ratios, where  $C_L = 1 \text{ mM}$ ,  $\sigma_1 = \sigma_2 = 10 \text{ mC m}^{-2}$  and  $L_1 = L_2 = 400 \text{ nm}$ .

then in the nanopore with  $R = 5 \text{ nm}$ . In Config. II, the concentration of  $\text{Na}^+$  shows an obvious drop at the nanopore junction due to the less significant degree of the EDL overlap in the large pore. At moderate concentration ratios, such as  $C_H/C_L = 100$ , the concentrations of  $\text{Na}^+$  and  $\text{Cl}^-$  at the nanopore junction take the same value, and then both decrease.

Fig. 3 shows the transference number, osmotic current, diffusive voltage, maximum power, and maximum power efficiency for different ionic diffusion directions at various concentration ratios. The transference numbers in both configurations decrease with increasing concentration ratio due to a lower EDL thickness at high concentrations, which hinders the selectivity of the bilayer channel. The transference number in Config. I is larger than that in Config. II due to a larger degree of EDL overlap in the small pore in contact with the low concentration reservoir, as shown in Fig. 3(a).

At low concentration ratios, the transference number is larger than 0.5, which means that the bilayer channel is cation selective, while at high concentration ratios, the transference number is less than 0.5, indicating that the bilayer channel is anion selective. At high concentration ratios, the ion transportation is governed by the diffusion effect induced by the large concentration gradient. As the diffusive coefficient of  $\text{Cl}^-$  is larger than that of  $\text{Na}^+$ , the co-ion flux is larger than the counter-ion flux. Hence the transference number is less than 0.5. A preferential ion transportation direction can also be observed in Fig. 4. The system presents an ionic rectification due to the asymmetric geometry, which is in accordance with the phenomenon observed in conical pores.<sup>30</sup> For nano-fluidic RED in conical nanopores in previous literature,<sup>20,21</sup> owing to the asymmetric geometry of the conical nanopore, the ion selectivity was larger when the low concentration was on the narrow side of the pore due to an addition in the EDL overlap near the tip side. In addition, Gao *et al.*<sup>12</sup> studied RED in an ionic diode membrane with heterojunctions between negatively charged mesoporous carbon (MesoC) (pore size  $\sim 7 \text{ nm}$ ) and positively charged macroporous alumina (MacroA) (pore size  $\sim 80 \text{ nm}$ ). That high concentration was present on the MacroC side induced a larger power density. This revealed that the optimal concentration gradient direction also depended on the signs of the charged walls. In the present study, the bilayer channel consists of large and small nanopores, which is, in some extent, similar to the conical geometry.

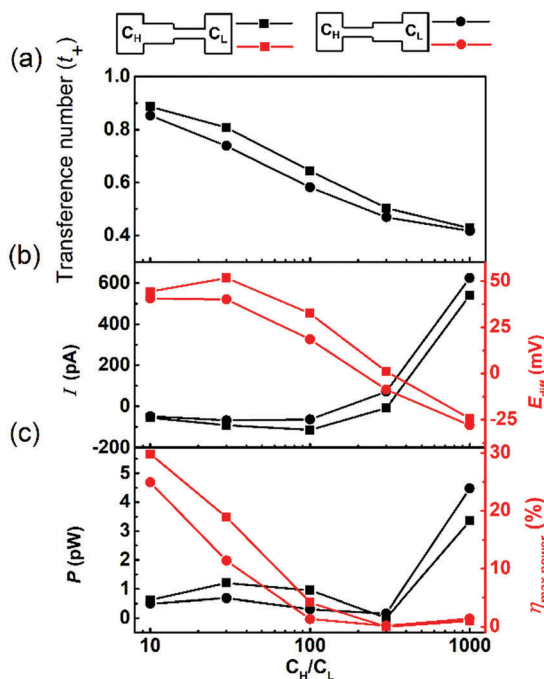


Fig. 3 Transference number, osmotic current, diffusive voltage, maximum power output and maximum power efficiency for different ionic diffusion directions, where  $C_L = 1 \text{ mM}$ ,  $\sigma_1 = \sigma_2 = 10 \text{ mC m}^{-2}$  and  $L_1 = L_2 = 400 \text{ nm}$ .

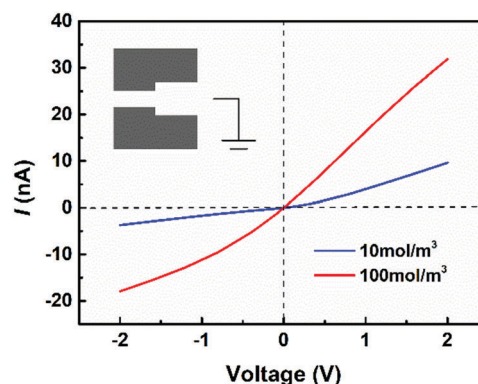


Fig. 4 Rectified ion transport through the bilayer nanochannel, where  $C_H = C_L = 10 \text{ mM}$  and  $100 \text{ mM}$ , and  $\sigma_1 = \sigma_2 = 10 \text{ mC m}^{-2}$ .

Therefore, the phenomenon of the RED in the negatively charged bilayer nanochannel is similar to that in the negatively charged conical nanopore: low concentration at the small pore side (Config. I) leads to larger ion selectivity.

As depicted in Fig. 3(b), the magnitude of osmotic current first increases with increasing  $C_H/C_L$  where the EDL overlap is dominant, then decreases as the diffusion effect augments. At high concentration ratios, the osmotic current shifts its sign and increases with increasing  $C_H/C_L$  as the diffusion coefficient of  $\text{Cl}^-$  is larger than that of  $\text{Na}^+$ , which increases with increasing concentration ratios. At low concentration ratios, the magnitude of the osmotic current in Config. I is larger than that in Config. II. An opposite phenomenon occurs at high concentration ratios due to the fact that ions can more easily diffuse through the nanopore with larger steric hindrance when in contact with the high concentration reservoir. The diffusive voltage first increases with increasing concentration ratio, reaches its maximum value, then decreases. Compared with the magnitude of  $C_H/C_L$ , the variation of  $\gamma_H/\gamma_L$  is rather small. Based on eqn (11),  $E_{\text{diff}}$  increases with increasing  $C_H/C_L$ , meanwhile the transference number decreases with increasing  $C_H/C_L$ . The increasing magnitude overrides the decreasing magnitude at a lower concentration ratio, while at higher concentration ratios the decreasing magnitude acts dominantly, which yields a maximum value of  $E_{\text{diff}}$ . In addition, at high concentration ratios, the nanochannel is anion selective, and the magnitude of  $E_{\text{diff}}$  in Config. II is larger than that in Config. I due to a lower transference number for  $\text{Na}^+$ .

According to the aforementioned discussion of the osmotic current and diffusive voltage, the maximum power has a maximum value at low concentration ratios, as shown in Fig. 3(c). According to eqn (14), the maximum power efficiency in Config. I is larger than that in Config. II, due to the larger transference number. At lower concentration ratios where the bilayer channel is cation selective, the maximum power efficiency decreases with increasing  $C_H/C_L$  due to the decreasing transference number. In the situations where the bilayer channel is anion selective, the maximum power efficiency increases slightly with increasing  $C_H/C_L$  as depicted in Fig. 3(c).

### Effects of asymmetric sub-nanopore length

To quantify the asymmetric degree of the bilayer channel length, the parameter  $\omega$  is defined as the percentage of the length of the small nanopore on the total length of the bilayer channel. A larger  $\omega$  means a larger length of the nanopore with  $R = 5$  nm.  $\omega = 0$  or  $\omega = 1$  indicates that the nanochannel solely consists of the nanopore with  $R = 10$  nm or  $R = 5$  nm, respectively.

As depicted in Fig. 5, the transference number increases with increasing  $\omega$  due to a more significant EDL overlap degree in small pores. At  $\omega = 0$  or  $\omega = 1$ , the bilayer channel returns to the single layer channel and the geometry is symmetric. Therefore, the transference number exhibits no difference in the two configurations. At  $0 < \omega < 1$ , the transference number in Config. I is always larger than that in Config. II, which has been explained in the previous section. As illustrated in Fig. 6(a), at very low concentration ratios, the osmotic current stays nearly stable at different  $\omega$  due to the relatively lower net charge density, so that the osmotic current in both configurations

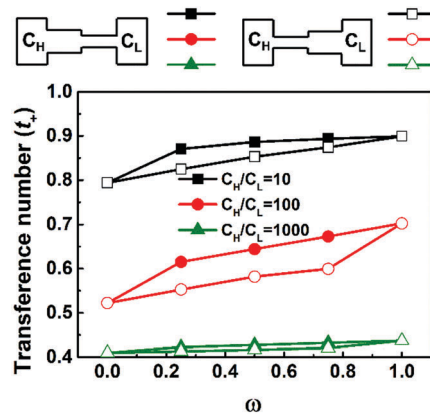


Fig. 5 Plot of transference number against  $\omega$  at different concentration ratios, where  $C_L = 1$  mM and  $\sigma_1 = \sigma_2 = 10$  mC m $^{-2}$ .

does not show an obvious difference. At moderate concentration ratios, the magnitude of osmotic current increases with increasing  $\omega$  due to a larger net charge density and significant EDL overlap degree in the small nanopore. At high concentration ratios where the ion transportation driven by the concentration gradient prevails, the osmotic current decreases with increasing  $\omega$  because of the augmentation of steric hindrance induced by the increasing length of the small nanopore. Based on eqn (11), the diffusive voltage with  $\omega$  presents the same trend with the transference number at lower  $C_H/C_L$ , as depicted in Fig. 6(b) where the diffusive voltage increases with increasing  $\omega$  due to the larger transference number. The maximum power follows the same trend. At high concentration ratios, the maximum power decreases with increasing  $\omega$  due to decreasing osmotic current and diffusive voltage, as shown in Fig. 6(c). According to eqn (14), the maximum power efficiency increases with increasing  $\omega$  in the cation selective regime (at low concentration ratios) and decreases with increasing  $\omega$  in the anion selective regime (at high concentration ratios), as depicted in Fig. 6(d).

### Effects of asymmetric surface charge density

The impacts of asymmetric surface charge densities at different sized pores on the transference number, osmotic current, and diffusive voltage are presented in Fig. 7. As shown in Fig. 7(a), for Config. I, the transference number is mainly determined by the surface charge density of the downstream small pore in contact with the low concentration reservoir where the EDL overlap is significant. Larger surface charge density of the downstream channel leads to a larger transference number. More intriguingly, we found that, at a very low concentration ratio ( $C_H/C_L = 10$ ), when the surface charge density of the small pore is fixed at  $10$  mC m $^{-2}$ , a lower surface charge density in the upstream large pore produces a larger value of transference number. This is because of the fact that at the pore junction section, the EDL overlap induced by the negatively charged wall of the upstream large pore impacts that induced by the downstream small pore. At lower concentrations, the ion transportation is dominated by the EDL overlap. Larger surface charge density results in a larger degree of EDL overlap in the upstream

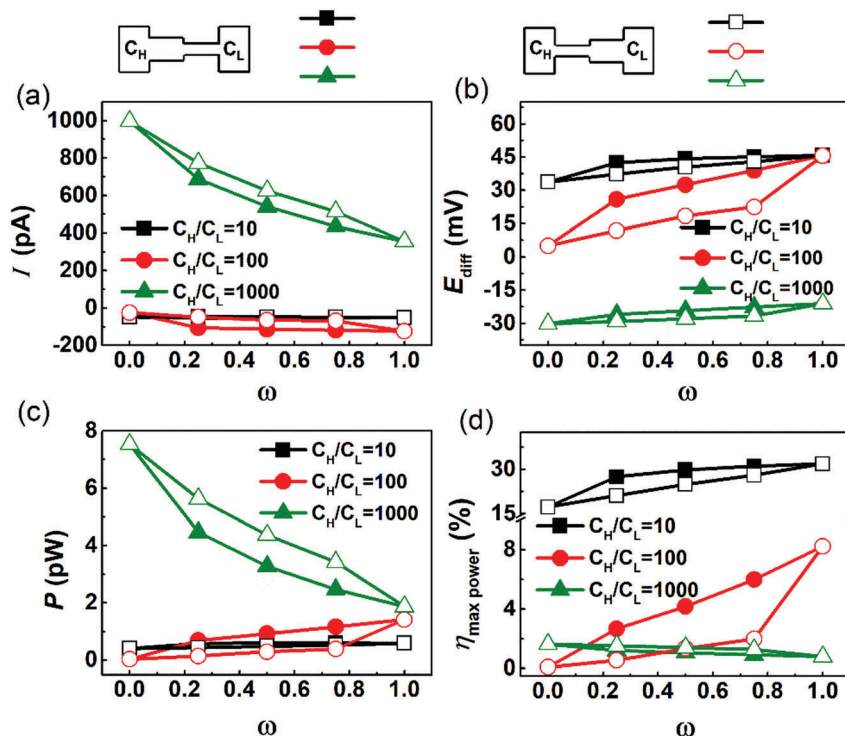


Fig. 6 Changes of osmotic current, diffusive voltage, maximum power and maximum power efficiency with  $\omega$  at different concentration ratios, where  $C_L = 1$  mM and  $\sigma_1 = \sigma_2 = 10$  mC m $^{-2}$ .

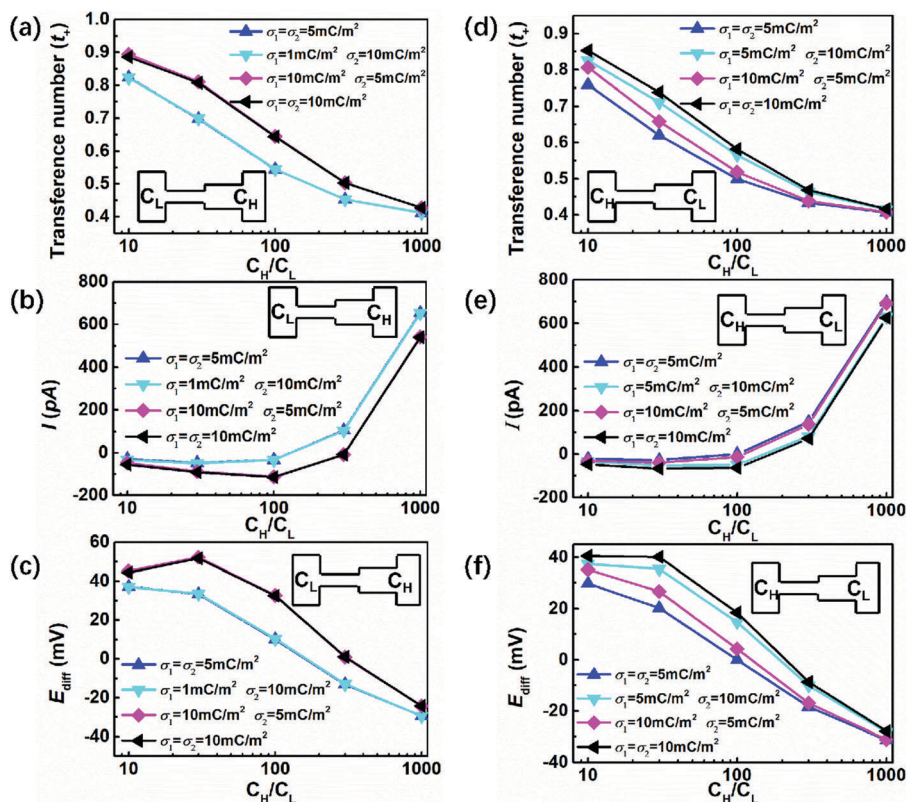


Fig. 7 Transference number, osmotic current, and diffusive voltage for different surface charge densities, where  $C_L = 1$  mM and  $L_1 = L_2 = 400$  nm.

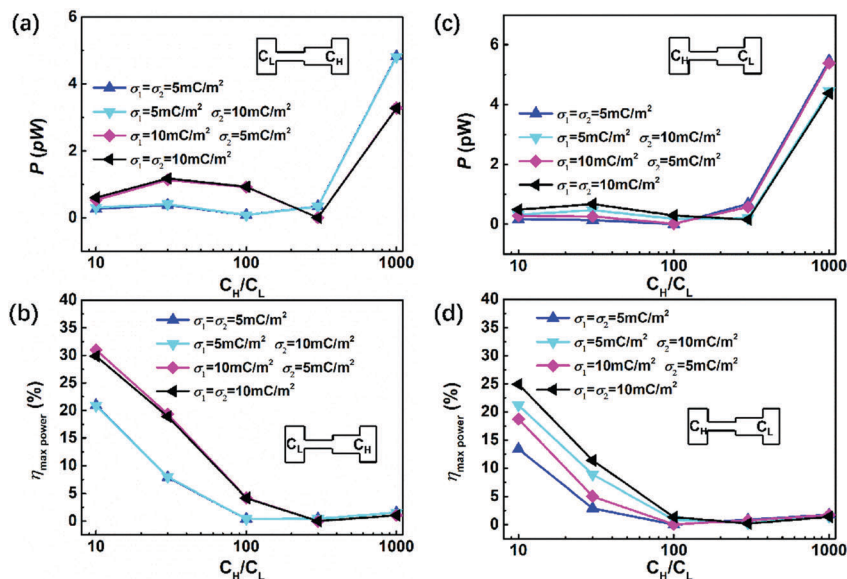


Fig. 8 Maximum power and maximum power efficiency for different surface charge densities, where  $C_L = 1$  mM and  $L_1 = L_2 = 400$  nm.

channel, which disturbs the EDL overlap in the downstream channel. Therefore, at the junction, the repulsion of the co-ions is weakened, and the concentration of  $\text{Cl}^-$  drops much more slowly at a larger surface charge density of the upstream large pore, as shown in Fig. 9. When the surface charge density of the downstream pore is small, the EDL overlap degree in the downstream channel is at a relatively lower level, and is not impacted by that induced by the upstream pore. Therefore, the selectivity stays unchanged, as shown in Fig. 7(a).

Fig. 7(b) demonstrates that the osmotic current also has the same value in modules that have identical surface charge density at the small pore. Larger surface charge density at the small pore leads to a larger magnitude of the osmotic current. As shown in Fig. 7(c), for a large surface charge density at the small pore wall, there exists an optimum concentration ratio that leads to the maximum value of the diffusive voltage. At small surface charge density, the diffusive voltage decreases consistently because of the fact that a much lower transference

number results in a significant decrease in diffusive voltage, which overrides the increasing impact induced by increasing  $C_H/C_L$ .

As shown in Fig. 7(d), a larger surface charge density at the downstream large pore leads to a larger transference number. Unlike the phenomenon in Config. I where the transference number is solely determined by the downstream small pore, the transference number in Config. II is also impacted by the surface charge density at the upstream small pore, a larger value of which leads to a larger transference number. The transference number in the module with a larger surface charge density at the small pore and a smaller one at the large pore is less than that in the module with the opposite surface charge density distribution. This is because in the small pore, high concentration induces a much thicker EDL, and the increase of charge density does not significantly contribute to the degree of the EDL overlap. In the large pore, the Debye length is much smaller than the radius, and increasing the charge density can obviously increase the EDL overlap degree, which contributes to the ion migration and thereby the transference number. As shown in Fig. 7(e) and (f), a larger surface charge density at the downstream large pore leads to a larger magnitude of the osmotic current and larger diffusive voltage due to the more significant degree of the EDL overlap.

For Config. I, the modules with the same surface charge density at the small pore present the same maximum power, and a larger surface charge density results in a larger value of the maximum power, as shown in Fig. 8. For Config. II, a larger surface density at the downstream large pore leads to a larger maximum power due to the larger diffusive voltage and osmotic current. For Config. I, at the concentration ratio of  $C_H/C_L = 10$ , due to the larger transference number, the maximum power efficiency in the module with  $10 \text{ mC m}^{-2}$  on the small pore and  $5 \text{ mC m}^{-2}$  on the large pore is larger than that of the module with the same surface charge density on the small pore and  $10 \text{ mC m}^{-2}$  on the large pore wall. However, it presents a

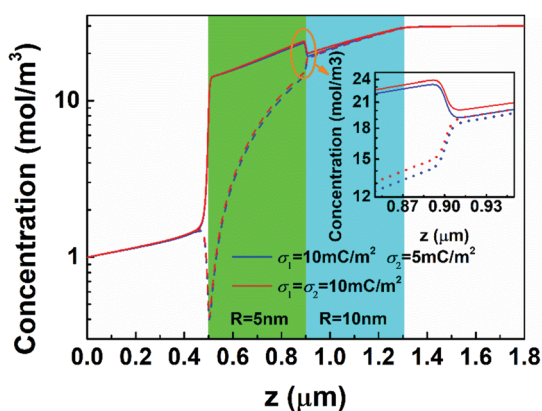


Fig. 9 Axial concentration distributions for symmetric surface charge densities at  $C_H/C_L = 10$  in Config. I, where  $C_L = 1$  mM and  $L_1 = L_2 = 400$  nm.

smaller maximum power induced by less osmotic current, as shown in Fig. 8(b).

## 4. Conclusions

To evaluate the possibility of a nano-fluidic RED system for salinity gradient energy harvesting, we focused on the behavior of ion transportation in a bilayer cylindrical nanochannel consisting of different sized nanopores connecting two large reservoirs at different NaCl concentrations. The impacts of ion diffusion direction, asymmetric pore length, surface charge density and bulk salt concentration ratio on the transference number, osmotic current, diffusive voltage, maximum power and maximum power efficiency were systematically investigated. The results can be summarized as follows: due to the asymmetric geometry of the bilayer channel, the performance of the nano-fluidic RED is impacted by the direction of the applied NaCl concentration gradient. The transference number of  $\text{Na}^+$  in Config. I is always larger than that in Config. II. At low concentration ratios, the magnitudes of osmotic current, diffusive voltage, maximum power and maximum power efficiency in Config. I are larger than those in Config. II, meanwhile the opposite phenomenon occurs at high concentration ratios. This is attributed to fact that the EDL overlap degree is more significant in Config. I and that high concentration hinders the thickness of the EDL. At low concentration ratios, the osmotic current and maximum power demonstrate maximum values, whereas the maximum power efficiency decreases consistently; at high concentration ratios, the maximum power increases obviously with increasing  $C_H/C_L$ , while the increase in the magnitude of the maximum power is rather small due to a large amount of Gibbs free energy consumed induced by large osmotic current. Furthermore, for symmetric surface charge densities, the ion transportation in Config. I is determined by the surface charge density at the downstream small nanopore, while for Config. II, it is significantly impacted by surface charge density at both sub-nanopores. For Config. I, when high surface charge is applied at the downstream small nanopore with a very low concentration, there exists an interesting phenomenon: larger surface charge density at the large nanopore induces a slight performance drop due to the impact of upstream EDL overlap.

## Conflicts of interest

There are no conflicts to declare.

## Acknowledgements

We acknowledge the support received from the National Natural Science Foundation of China (51706076, 51736004).

## References

- 1 R. Long, Y. J. Bao, X. M. Huang and W. Liu, *Energy*, 2014, **73**, 475–483.
- 2 R. Long, B. Li, Z. Liu and W. Liu, *Energy*, 2015, **93**, 2079–2086.
- 3 R. Long, B. Li, Z. Liu and W. Liu, *Energy*, 2015, **87**, 463–469.
- 4 A. Achilli, A. E. Childress and T. Y. Cath, *J. Membr. Sci.*, 2009, **343**, 42–52.
- 5 A. M. Weiner, R. K. McGovern and H. L. V. John, *J. Membr. Sci.*, 2015, **493**, 605–614.
- 6 R. A. Tufa, E. Curcio, E. Brauns, W. van Baak, E. Fontananova and G. Di Profio, *J. Membr. Sci.*, 2015, **496**, 325–333.
- 7 J. Liu, G. M. Geise, X. Luo, H. Hou, F. Zhang, Y. Feng, M. A. Hickner and B. E. Logan, *J. Power Sources*, 2014, **271**, 437–443.
- 8 R. Elfrink, T. M. Kamel, M. Goedbloed, S. Matova, D. Hohlfeld, Y. van Andel and R. van Schaijk, *J. Micromech. Microeng.*, 2009, **19**, 094005.
- 9 R. Long, B. Li, Z. Liu and W. Liu, *J. Membr. Sci.*, 2017, **525**, 107–115.
- 10 A. Esfandiari, B. Radha, F. Wang, Q. Yang, S. Hu, S. Garaj, R. Nair, A. Geim and K. Gopinadhan, *Science*, 2017, **358**, 511–513.
- 11 J. Hwang, S. Kataoka, A. Endo and H. Daiguji, *Lab Chip*, 2016, **16**, 3824–3832.
- 12 J. Gao, W. Guo, D. Feng, H. Wang, D. Zhao and L. Jiang, *J. Am. Chem. Soc.*, 2014, **136**, 12265.
- 13 D.-K. Kim, C. Duan, Y.-F. Chen and A. Majumdar, *Microfluid. Nanofluid.*, 2010, **9**, 1215–1224.
- 14 J. Kim, S. J. Kim and D. K. Kim, *Energy*, 2013, **51**, 413–421.
- 15 K. L. Liu, J. P. Hsu and S. Tseng, *Langmuir*, 2013, **29**, 9598–9603.
- 16 P. B. Peters, R. R. Van, M. Z. Bazant and P. M. Biesheuvel, *Phys. Rev. E*, 2016, **93**, 053108.
- 17 L. H. Yeh, M. Zhang, S. Qian and A. Chem, *Anal. Chem.*, 2013, **85**, 7527.
- 18 L. H. Yeh, M. Zhang, S. Qian and J. P. Hsu, *Nanoscale*, 2012, **4**, 2685–2693.
- 19 Y. Ai, M. Zhang, W. J. Sang, M. A. Cheney and S. Qian, *J. Phys. Chem. C*, 2013, **114**, 3883–3890.
- 20 W. Guo, L. Cao, J. Xia, F. Q. Nie, W. Ma, J. Xue, Y. Song, D. Zhu, Y. Wang and L. Jiang, *Adv. Funct. Mater.*, 2010, **20**, 1339–1344.
- 21 H. C. Yeh, C. C. Chang and R. J. Yang, *RSC Adv.*, 2013, **4**, 2705–2714.
- 22 J.-P. Hsu, S.-C. Lin, C.-Y. Lin and S. Tseng, *J. Power Sources*, 2017, **366**, 169–177.
- 23 J. Hwang, T. Sekimoto, W.-L. Hsu, S. Kataoka, A. Endo and H. Daiguji, *Nanoscale*, 2017, **9**, 12068–12076.
- 24 L. H. Yeh, C. Hughes, Z. Zeng and S. Qian, *Anal. Chem.*, 2014, **86**, 2681–2686.
- 25 S. Tseng, Y. M. Li, C. Y. Lin and J. P. Hsu, *Nanoscale*, 2016, **8**, 2350.
- 26 L. Cao, W. Guo, W. Ma, L. Wang, F. Xia, S. Wang, Y. Wang, L. Jiang and D. Zhu, *Energy Environ. Sci.*, 2011, **4**, 2259–2266.
- 27 B. D. Kang, H. J. Kim, M. G. Lee and D. K. Kim, *Energy*, 2015, **86**, 525–538.
- 28 Z. Zhang, X. Sui, P. Li, G. Xie, X. Y. Kong, K. Xiao, L. Gao, L. Wen and L. Jiang, *J. Am. Chem. Soc.*, 2017, **139**, 8905.
- 29 L. A. Bromley, *AIChE J.*, 1973, **19**, 313–320.
- 30 J. Cervera, A. Alcaraz, B. Schiedt, R. Neumann and P. Ramírez, *J. Phys. Chem. C*, 2007, **111**, 12265.